



Excellent photo-Fenton catalysts of Fe–Co Prussian blue analogues and their reaction mechanism study

Xuning Li^{a,b}, Jiayi Liu^{a,b}, Alexandre I. Rykov^a, Hongxian Han^c, Changzi Jin^a, Xin Liu^a, Junhu Wang^{a,*}

^a Mössbauer Effect Data Center & Laboratory of Catalysts and New Materials for Aerospace, Dalian Institute of Chemical Physics, Chinese Academy Sciences, Dalian 116023, China

^b University of Chinese Academy of Sciences, Beijing 100049, China

^c Division of Solar Energy, Dalian National Laboratory for Clean Energy & State Key Laboratory of Catalysis, Dalian Institute of Chemical Physics, Chinese Academy of Sciences, Dalian 116023, China

ARTICLE INFO

Article history:

Received 30 December 2014

Received in revised form 17 April 2015

Accepted 14 May 2015

Available online 15 May 2015

Keywords:

Fe–Co Prussian blue

Mössbauer spectroscopy

Heterogeneous Fenton mechanism

Water coordinated iron

Singlet oxygen

ABSTRACT

Two kinds of Fe–Co Prussian blue analogues (Fe–Co PBAs) with different iron valence state, $\text{Fe}_3[\text{Co}(\text{CN})_6]_2 \cdot 12\text{H}_2\text{O}$ and $\text{Fe}[\text{Co}(\text{CN})_6] \cdot 2\text{H}_2\text{O}$, were developed as the photo-Fenton catalysts for in-depth investigation of the heterogeneous Fenton reaction mechanism. These two catalysts showed exceptionally high efficiencies for the degradation of Rhodamine B. The efficient redox cycling of iron species in the Fe–Co PBAs photo-Fenton process was deeply explored by Mössbauer spectroscopy. The excellent photo-Fenton activities of these Fe–Co PBAs were ascribed to the existence of highly dispersed water coordinated iron sites and abundant vacancies in the metal-organic-frameworks. Singlet oxygen was identified by radical scavenger experiments and electron paramagnetic resonance spectroscopy, which plays a key role in the photo-Fenton process. Based on these comprehensive experimental results, a novel radical reaction mechanism was proposed. This work not only opens up a new avenue for the application of Fe–Co PBAs, but also gives a deeper insight into the mechanisms of heterogeneous Fenton reactions.

© 2015 Elsevier B.V. All rights reserved.

1. Introduction

Nowadays, the scarcity of fresh water resources and the ever-growing environmental pollution have been attracting increased concern [1]. Toxic organic pollutants in the wastewater which adversely affect the health of human beings must be reduced to acceptable level [2–4]. Over the past few years, various wastewater treatment techniques have been developed, such as absorption and filtration processes [5], biological degradation [6], advanced oxidation processes (AOPs) [7], and so on. The heterogeneous Fenton process has been widely investigated due to its high efficiency in removing persistent organic contaminants with lower amounts of H_2O_2 consumption under a wide pH range [8–10]. Most of the recent researches concentrate on the modification of the iron minerals and design of heterogeneous Fenton-like catalysts with high activity and durability [11–13]. However, limited mechanism understanding hinders the breakthroughs in Fenton chemistry. In most cases, the relationship between the catalyst structure, the effi-

ciency of active radical (such as $\cdot\text{OH}$) generation, and the redox cycling process of iron species are still unclear [10,14–15]. For instance, Purceno et al. reported the oxidation of Fe^{II} after the Fenton process [16]. However, Yang et al. observed the opposite process, in which Fe^{III} was reduced after the Fenton reaction [14]. In order to understand the mechanisms of the heterogeneous Fenton reactions, it is vitally important to clarify the structure changes of the catalyst and the redox cycling of the iron species during the whole reaction process.

^{57}Fe Mössbauer spectroscopy is a unique method for determining the oxidation state and the coordination environment of iron species in solids [17]. In our previous study, the synergistic effects of TiO_2 photocatalyst and Prussian blue (PB, $\text{Fe}_3[\text{Fe}(\text{CN})_6]_4 \cdot 14\text{H}_2\text{O}$) Fenton-like system were demonstrated by Mössbauer technique [18]. Therefore, Mössbauer spectroscopy is a powerful technique for the study of the Fenton process. $\text{Fe}_3[\text{Co}(\text{CN})_6]_2 \cdot 12\text{H}_2\text{O}$ and $\text{Fe}[\text{Co}(\text{CN})_6] \cdot 2\text{H}_2\text{O}$ ($\text{Fe}^{\text{II}}\text{--Co}$ and $\text{Fe}^{\text{III}}\text{--Co}$ PBA) are Prussian blue analogues which exhibit some functional properties, such as striking photo-magnetic [19], hydrogen storage [20], zero thermal expansion [21], and catalytic properties [22,23]. Fe–Co PBAs are in a kind of metal-organic-framework (MOF) structure constructed by octahedral $[\text{Co}(\text{CN})_6]^{3-}$ anion groups bridged with iron ions to form

* Corresponding author. Tel.: +86 411 84379159; fax: +86 411 84685940.

E-mail address: wangjh@dicp.ac.cn (J. Wang).

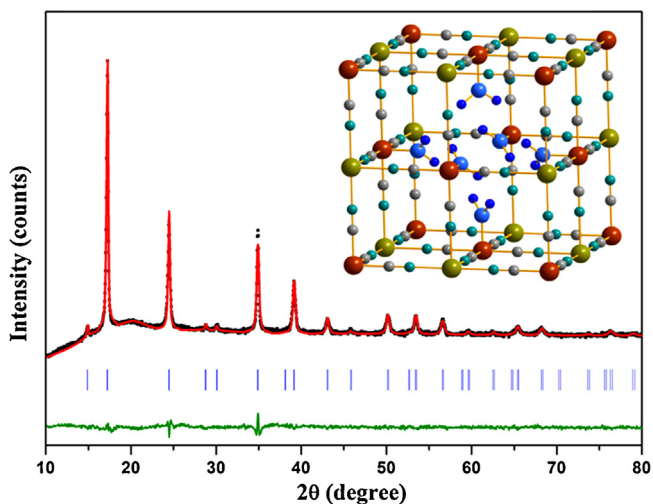


Fig. 1. Results of the Rietveld refinement for $\text{Fe}_3[\text{Co}(\text{CN})_6]_2 \cdot 12\text{H}_2\text{O}$ ($a = 10.282 \text{\AA}$, space group Fm-3m, $R_{\text{wp}} = 12.5\%$, $R_{\text{exp}} = 8.62\%$). The tic marks display the reflection positions, and the lower solid line displays the difference profile. (Inset: Cubic MOFs structure of $\text{Fe}_3[\text{Co}(\text{CN})_6]_2 \cdot 12\text{H}_2\text{O}$ with vacancies and water coordinated iron sites.)

simple cubic lattice structure [24]. The charge balance in the crystal structure is achieved by random distribution of the $[\text{Co}(\text{CN})_6]^{3-}$ vacancies, leading to the coordination of Fe^{II} or Fe^{III} centers with one or several water molecules as shown in the inset picture of Fig. 1 [25]. The existence of abundant vacancies and water coordinated iron sites in the MOFs structure may be beneficial for the Fe–Co PBAs in the Fenton process. However, there is no report on the application of Fe–Co PBAs in Fenton chemistry to date.

In this work, we studied the catalytic properties of the Fe–Co PBAs ($\text{Fe}^{\text{II}}\text{–Co}$ and $\text{Fe}^{\text{III}}\text{–Co}$) in heterogeneous Fenton reactions with particular emphasis on the underlying reaction mechanism. Extensive investigations have been carried out on the Fenton activities of Fe–Co PBAs, including the degradation of model pollutant Rhodamine B (RhB) under various conditions, the stability of the Fe–Co PBAs in the photo-Fenton process, the redox cycling of iron species and the photo-Fenton mechanisms of Fe–Co PBAs explored by ^{57}Fe Mössbauer spectroscopy. Singlet oxygen was identified by radical scavenger experiments and electron paramagnetic resonance (EPR) spectroscopy, which plays a key role in the photo-Fenton process. Relevant radical reaction pathways in photo-Fenton process were proposed.

2. Experimental

2.1. Materials and chemicals

Potassium hexacyanocobaltate(III) (98%) was purchased from Beijing J&K Co., Ltd., China. Sodium azide, p-benzoquinone (BQ), 5,5-dimethyl-1-pyrroline-N-oxide (DMPO) and iron oxide (II, III) (99.5%, ~20 nm) were purchased from Aladdin Co., China and RhB was acquired from Sigma-Aldrich. Ferric chloride, ferrous chloride, cobaltous chloride, copper chloride, potassium ferrocyanide, *t*-butanol (TBA) and 30% hydrogen peroxide aqueous solution were purchased from Tianjin Kermel Chemical Reagent Co., Ltd., China. All chemical reagents were used without further purification.

2.2. Preparation of Fe–Co PBAs

$\text{Fe}_3[\text{Co}(\text{CN})_6]_2 \cdot 12\text{H}_2\text{O}$ ($\text{Fe}^{\text{II}}\text{–Co PBA}$) and $\text{Fe}[\text{Co}(\text{CN})_6] \cdot 2\text{H}_2\text{O}$ ($\text{Fe}^{\text{III}}\text{–Co PBA}$) were prepared by reaction of aqueous solutions of $\text{FeCl}_2 \cdot 4\text{H}_2\text{O}$ or $\text{FeCl}_3 \cdot 6\text{H}_2\text{O}$ and $\text{K}_3[\text{Co}(\text{CN})_6]$. The preparation process was similar to previous reports [21,26] but with slight mod-

ification. Typically, 25 mL $\text{K}_3[\text{Co}(\text{CN})_6]$ aqueous solution (0.10 M) was slowly added into 25 mL $\text{FeCl}_2 \cdot 4\text{H}_2\text{O}$ or $\text{FeCl}_3 \cdot 6\text{H}_2\text{O}$ aqueous solution (0.10 M) under magnetic stirring. The mixed solution was further stirred for another 30 min and aged for 1 day. Finally, the resulting precipitates were centrifuged and washed for at least three times with deionized water, followed by drying in an oven at 333 K for 12 h. For comparison, the insoluble PB sample was synthesized by the same process as that of $\text{Fe}^{\text{III}}\text{–Co PBA}$, except the replacement of $\text{K}_3[\text{Co}(\text{CN})_6]$ (0.10 M) using $\text{K}_4[\text{Fe}(\text{CN})_6] \cdot 3\text{H}_2\text{O}$ (0.15 M). The $\text{Cu}_3[\text{Co}(\text{CN})_6]_2$ ($\text{Cu}^{\text{II}}\text{–Co PBA}$) and $\text{Co}_3[\text{Co}(\text{CN})_6]_2$ ($\text{Co}^{\text{II}}\text{–Co PBA}$) were also synthesized by the similar process but with $\text{CuCl}_2 \cdot 2\text{H}_2\text{O}$ and $\text{CoCl}_2 \cdot 6\text{H}_2\text{O}$ as the metal precursors, respectively.

2.3. Characterization of Fe–Co PBAs

The X-ray diffraction (XRD) patterns were measured on a PANalytical X'Pert-Pro X-ray diffractometer equipped with Ni-filtered $\text{Cu K}\alpha$ ($\lambda = 0.15406 \text{ nm}$) radiation source in an angular range of 2θ from 10° to 80° . The structural refinements were conducted by the Rietveld method using the FULLPROF software based on the XRD data. The surface morphologies were studied using a Tecnai G² Spirit transmission electron microscopy (TEM) with an accelerating voltage of 120 kV. The specific surface areas were analyzed by the Brunauer–Emmett–Teller (BET) N_2 adsorption–desorption method on a Micromeritics ASAP 2010 instrument at 77 K, and the pore size distributions were analyzed using the Barrett–Joyner–Halenda (BJH) method from the desorption branch of the N_2 adsorption–desorption isotherms. Fourier transform infrared spectra (FT-IR) were recorded on a Bruker spectrometer equipped with a MCT detector in the region of $400\text{--}4000 \text{ cm}^{-1}$ at a resolution of 4 cm^{-1} . The thermo-gravimetric and differential scanning calorimetry (TG-DSC) analyses were carried out using a Setaram Setsys 16/18 thermo-analyzer at a heating rate of 2°C min^{-1} in N_2 flow. The X-ray photoelectron spectra (XPS) were measured on an ESCALAB 250 X-ray photoelectron microscope equipped with monochromated $\text{Al K}\alpha$ source. All binding energies were calibrated by a standard sample of contaminated carbon (C 1s = 284.6 eV). The spectra were fitted by the XPSPEAK41 software using Shirley-type background.

The room temperature ^{57}Fe Mössbauer spectra were recorded using a proportional counter and a Topologic 500A spectrometer with $^{57}\text{Co}(\text{Rh})$ as a γ -ray radioactive source. The EPR spectra carried out in the Fenton process were obtained using a Bruker ESR I200 spectrometer with the sweep width of 100 G and a center field at 3320 G at room temperature. The detailed procedures of Mössbauer and EPR measurements can be found in our previous work [18].

2.4. Catalytic activity measurements of Fe–Co PBAs

The Fenton performance of Fe–Co PBAs was tested by the degradation of RhB dye (12 mg L^{-1}) with H_2O_2 (4 mM) at pH 4.8 (initial pH of RhB aqueous solution) in a dark box. If necessary, the pH value was adjusted by either 0.1 M HNO_3 or NaOH aqueous solution and recorded with an Orion pH meter (model PHSJ-3F). The temperature was kept at 308 K using a water bath. The concentrations of leached iron and cobalt in solution were measured by Thermo IRIS Intrepid II inductively coupled with plasma-optical emission spectroscopy (ICP-OES).

In all experiments, 10 mg Fe–Co PBAs were added into a 50 mL RhB solution (12 mg L^{-1}) and stirred for 30 min to establish the adsorption–desorption equilibrium. The reaction was initiated by adding certain amounts of H_2O_2 aqueous solution and simultaneously turning on the Xenon lamp (MAX-303, Asahi Spectra Co., Ltd.) equipped with a 400 nm long-pass filter (light intensity: $\sim 13.3 \text{ mW cm}^{-2}$, the photo emission spectrum of the lamp can be found in our previous work [18]). During the reaction, 2 mL

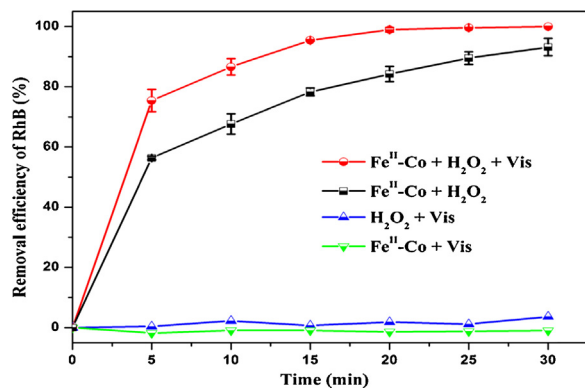


Fig. 2. The performance of $\text{Fe}_3[\text{Co}(\text{CN})_6]_2 \cdot 12\text{H}_2\text{O}$ ($\text{Fe}^{\text{II}}\text{-Co PBA}$) in different systems. Reaction conditions: $[\text{RhB}] = 12 \text{ mg L}^{-1}$, $[\text{H}_2\text{O}_2] = 4 \text{ mM}$, catalyst $= 0.2 \text{ g L}^{-1}$, $T = 308 \text{ K}$, pH 4.8 and MAX-303 Xenon lamp: 13.5 mW cm^{-2} .

of the reaction mixture were taken out at certain time interval and centrifuged before measuring the UV-vis absorption spectra. The homogeneous photo-Fenton reaction was carried out for comparison using $\text{FeCl}_3 \cdot 6\text{H}_2\text{O}$ as the iron source (same iron concentration as that of $\text{Fe}^{\text{II}}\text{-Co PBA}$). The degradation of RhB was monitored by the changes of the RhB absorption peak at 553 nm in the UV-vis spectra (Cintra spectrophotometer, GBC, Australia). The mineralization of RhB was checked by a total organic carbon analyzer (TOC-VCPh/CPN, Shimadzu, Japan). In each recyclability test, the catalyst was centrifuged and washed thoroughly with deionized water, followed by drying at 60°C . The dark Fenton and photo-Fenton reaction activities were calculated by the following equations:

$$\text{Decolorization efficiency} (\%) = [(C_0 - C_t)/C_0] \times 100$$

$$\ln(C_0/C_t) = kt$$

where C_0 is the initial dye concentration reached adsorption-desorption equilibrium in dark, C_t is the dye concentration at certain time t during the Fenton process, and k is the reaction rate constant.

3. Results and discussion

3.1. Catalytic activity of Fe-Co PBAs

Fig. 2 shows the photo-Fenton properties of $\text{Fe}^{\text{II}}\text{-Co PBA}$ under different reaction conditions. Neither $\text{Fe}^{\text{II}}\text{-Co/Vis}$ nor $\text{H}_2\text{O}_2\text{/Vis}$ could effectively degrade RhB. The removal efficiency of RhB by $\text{Fe}^{\text{II}}\text{-Co/H}_2\text{O}_2$ was 93% in 30 min. The activity was largely increased to 100% in 20 min with the assistance of visible light irradiation. This excellent photo-Fenton activity of $\text{Fe}^{\text{II}}\text{-Co PBA}$ is comparable to several other known Fenton catalysts as shown in **Fig. 3**. Many of the recent researches were focused on modifying nano- Fe_3O_4 to increase its Fenton property [8,11,27,28]. In our experimental conditions, however, the removal efficiency of RhB by nano- Fe_3O_4 was only 4% in 30 min. Compared to $\text{Fe}^{\text{II}}\text{-Co PBA}$, the $\text{Fe}^{\text{III}}\text{-Co PBA}$ is relatively less active but it can still reach the RhB removal efficiency of 65% within 30 min. The main reason for such high activity is possibly due to its versatile porous structure with abundant octahedral iron sites with mixed valences [27]. The RhB degradation efficiency by PB was only 20% under the same experimental conditions, which is much smaller than 65% of $\text{Fe}^{\text{III}}\text{-Co PBA}$ (**Fig. 3a**). This might be due to relatively smaller surface area of PB ($8.4 \text{ m}^2 \text{ g}^{-1}$) than that of the $\text{Fe}^{\text{III}}\text{-Co PBA}$ ($23.7 \text{ m}^2 \text{ g}^{-1}$) as shown in **Table 1**. The photo-Fenton activity of $\text{Fe}^{\text{II}}\text{-Co PBA}$ at pH 4.8 was comparable to that of the homogeneous photo-Fenton reaction ($\text{Fe}^{3+}/\text{H}_2\text{O}_2$) at pH 4.0.

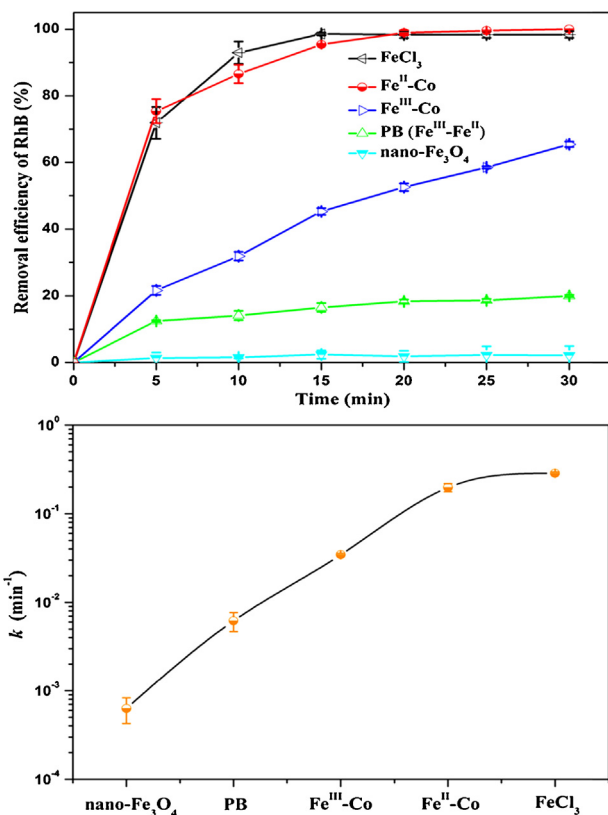


Fig. 3. The photo-Fenton activities (a) and rate constants (b) of Fe-Co PBAs compared with that of nano- Fe_3O_4 , PB and FeCl_3 homogenous systems. Reaction conditions: $[\text{RhB}] = 12 \text{ mg L}^{-1}$, $[\text{H}_2\text{O}_2] = 4 \text{ mM}$, catalyst $= 0.2 \text{ g L}^{-1}$, $T = 308 \text{ K}$, the initial pH of homogenous system 4.0 and the others 4.8, MAX-303 Xenon lamp: 13.5 mW cm^{-2} .

Table 1

The textural structural parameters of the Fe-Co PBAs, PB and nano- Fe_3O_4 analyzed by the BET N_2 adsorption-desorption method.

	Fe ^{II} -Co	Fe ^{II} -Co used	Fe ^{III} -Co	PB	Fe ₃ O ₄
BET surface area ($\text{m}^2 \text{ g}^{-1}$)	199	158	24	8	7
Average pore diameter (nm)	2.1	2.1	1.6	1.8	1.7

The relevant rate constants of the different reaction systems were shown in **Fig. 3b**. The RhB degradation activities over Fe-Co PBAs via the photo-Fenton oxidation process are even much higher than those of the catalysis recently reported in the literatures (Table S1) [29–32].

3.2. Characterization of catalysts and the mechanism study

3.2.1. Characterization of catalysts by XRD, BET, TG-DSC, FT-IR, TEM, and XPS

To understand the mechanisms of Fe-Co PBAs photo-Fenton process, it is important to clarify the structure change of the catalyst and the redox cycling of the iron species during the whole reaction process. To this end, a number of techniques were applied for the catalysts characterization.

The XRD patterns of Fe-Co PBAs before and after the Fenton reaction are shown in **Fig. 4a**. The (111), (200), (220), (400), (331), and (422) characteristic diffraction peaks of $\text{Fe}_3[\text{Co}(\text{CN})_6]_2 \cdot 12\text{H}_2\text{O}$ can be clearly observed (JCPDS No. 89-3736). The characteristic diffraction peaks of $\text{Fe}^{\text{II}}\text{-Co PBA}$ are similar to those of $\text{Fe}^{\text{II}}\text{-Co PBA}$, except a slight shift of the peak positions towards higher angles. Similar shifts were also observed for $\text{Fe}^{\text{II}}\text{-Co PBA}$ after photo-Fenton reaction, indicating the oxidation of Fe^{II} .

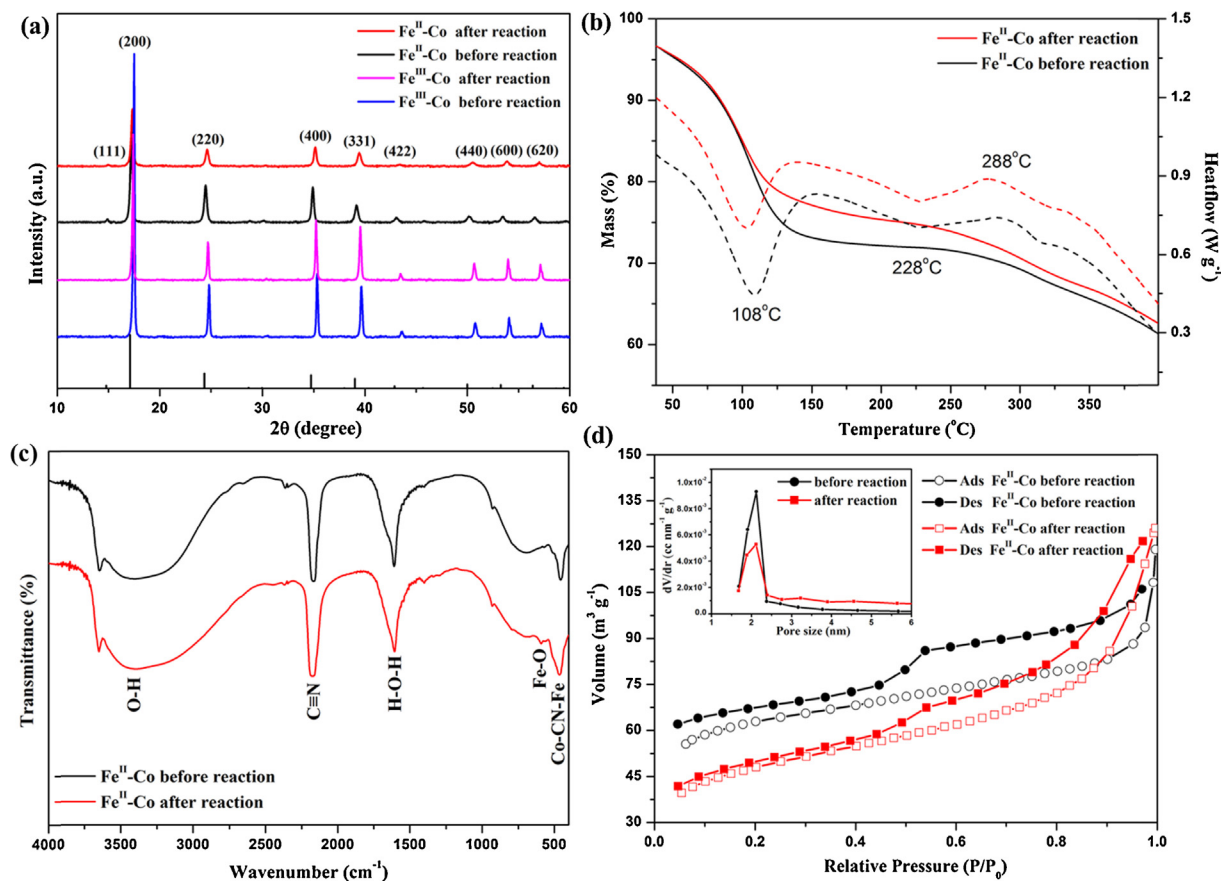


Fig. 4. Characterizations of (a) Fe-Co PBAs by XRD; Fe^{II}-Co PBA by (b) TG-DSC; (c) FT-IR; (d) BET N₂ adsorption–desorption method (insert: pore size distribution) before and after photo-Fenton reaction.

to Fe^{III} during the photo-Fenton process. However, the XRD patterns of Fe^{III}-Co PBA before and after photo-Fenton reaction were almost the same (Fig. 4a), indicating that there were no detectable changes in its crystal structure after the photo-Fenton process. Taking into consideration that the similar morphologies of Fe^{III}-Co PBA before and after the photo-Fenton reaction as observed by TEM (Fig. 5), it could be concluded that Fe^{III}-Co PBA is more stable compared to Fe^{II}-Co PBA, since the later is more readily oxidized during the Fenton process. Fe^{II}-Co PBA has an average pore size diameter of 2.1 nm, which showed no changes before and after Fenton reaction (Fig. 4d). This is in agreement with the existence of extended pores formed by the aggregation of the [Co(CN)₆]³⁻ vacancies as shown in Fig. S1. The BET surface area of Fe^{II}-Co PBA (Table 1) showed a slight decrease after the Fenton reaction, which might be due to the crystallization of a new phase on the surface of Fe^{II}-Co PBA nanoparticles as confirmed by TEM (Fig. 5). However, the surface area of Fe^{II}-Co PBA after the Fenton reaction still remained much larger than that of PB [20]. Furthermore, the pore sizes changed little in the course of Fenton reaction, suggesting that the metal-cyanide-frameworks remained intact after the photo-Fenton process. TG-DSC curves show that the weight loss of samples took place in different stages (Fig. 4b). A weight loss of 27% and 24% in the first stage (below 150 °C) was recorded for Fe^{II}-Co samples before and after reaction, which is due to the removal of the crystalline water molecules. The loss of weight in the second stage (150–280 °C) and the third stage (over 280 °C) was due to the removal of the coordinated water molecules and the decomposition of the organic ligands (C≡N), respectively [33]. The slight change observed in the TG-DSC curves before and after the reaction could be related to the generation of a new Fe–O phase (Fe

oxide and/or hydroxide phases). Fig. 4c shows the FT-IR spectra of the two samples before and after the reaction. The absorption band at 2166 cm⁻¹ is characteristic of the CN stretching vibration of PBA [34]. The absorption bands of H–O–H bending mode at 1610 and O–H stretching mode at 3390 cm⁻¹ [35] demonstrate the presence of water molecules in the MOF structure of Fe^{II}-Co PBA, which is in well accordance with the TG-DSC results. The small band at 590 cm⁻¹ emerged after the reaction could be assigned to the new Fe–O phase formed on the surface of Fe^{II}-Co PBA nanoparticles [36]. However, no significant changes were observed in FT-IR spectra of the Fe^{II}-Co PBA before and after the reaction, indicating that its crystal structure was stable during the photo-Fenton process.

The surface element compositions and the valence states of the catalysts were revealed by XPS (Fig. 6). Based on the full XPS spectrum shown in Fig. 6a, the surface O/Fe/Co molar ratio of 1.27/1.14/1 and 3.27/1.40/1 were obtained for Fe^{II}-Co PBA before and after the photo-Fenton reaction, respectively. The increase in contents of the surface Fe and O species after reaction supports generation of a new Fe–O phase on the surface of Fe^{II}-Co PBA nanoparticles. In the high resolution XPS of Fe 2p_{3/2} of Fe^{II}-Co PBA (Fig. 6b), the binding energies of Fe 2p_{3/2} at 709.2 eV and 711.1 eV correspond to Fe^{II} and Fe^{III}, respectively [37]. The new peak appeared at 712.7 eV and the corresponding changes observed in the high resolution XPS of O 1s (Fig. 6d) confirm that the Fe–O species were truly produced on the surface of the Fe^{II}-Co PBA nanoparticles during the photo-Fenton process [38]. The oxidation of Fe^{II} in the Fe^{II}-Co PBA Fenton reaction was also evidenced by XPS (Fig. 6b). However, no obvious change was observed in the high resolution XPS of Co 2p_{3/2} (Fig. 6c), indicating that the excellent photo-Fenton activity of Fe^{II}-Co PBA mainly originates from Fe^{II} and Fe^{III} in its MOF structure.

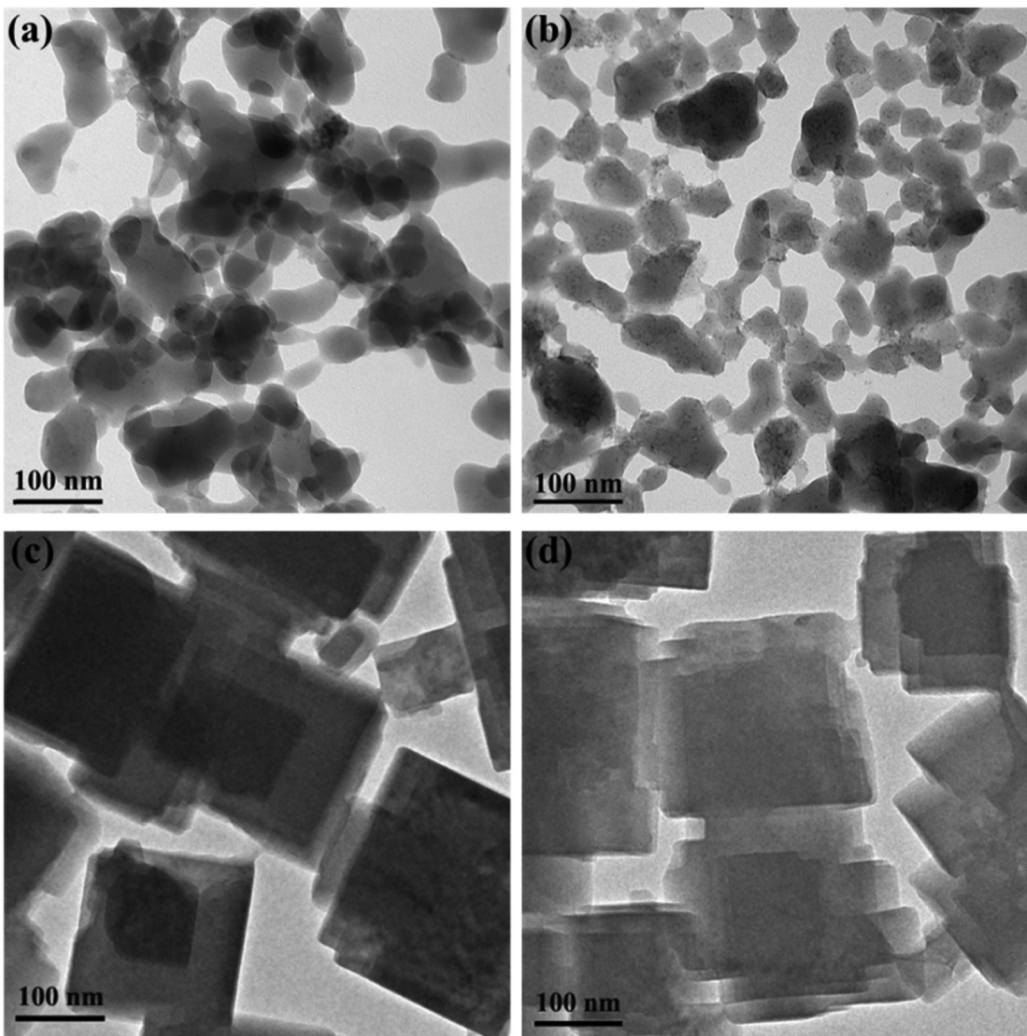


Fig. 5. TEM images of $\text{Fe}^{\text{II}}\text{-Co PBA}$: (a) before, (b) after; $\text{Fe}^{\text{III}}\text{-Co PBA}$: (c) before, and (d) after photo-Fenton reactions.

To further clarify the role of Fe and Co in Fe–Co PBAs in the photo-Fenton process, contrast experiments of the Fenton activities of the M^{II} –Co PBAs ($M = \text{Fe, Co, Cu}$) were carried out (Fig. S2). Results show that the activity of $\text{Fe}^{\text{II}}\text{-Co PBA}$ was much higher than that of $\text{Cu}^{\text{II}}\text{-Co PBA}$ and $\text{Co}^{\text{II}}\text{-Co PBA}$. This further confirms that the excellent Fenton activity originates mainly from the Fe in its MOF structure.

3.2.2. Characterizations of catalysts by Mössbauer spectroscopy and plausible mechanisms of the photo-Fenton reaction over Fe–Co PBAs catalysts

In order to investigate the iron redox cycling and the mechanisms of the photo-Fenton processes over Fe–Co PBA catalysts, ^{57}Fe Mössbauer spectroscopy was applied to determine the oxidation state and coordination environment of iron ions in Fe–Co PBAs under different Fenton reaction conditions (Fig. 7). The fitting model of the spectra was same as a previous work to a similar PBA complex [39,40]. The obtained Mössbauer isomer shifts of $\text{Fe}^{\text{II}}\text{-Co PBA}$ (Fig. 7a) suggest that 89% of the Fe species are in high-spin Fe^{II} (Table 2). In this porous structure with rich of water coordinated Fe (Fe–water), majority of the $\text{Fe}^{\text{II}}/\text{Fe}^{\text{III}}$ species are octahedrally coordinated by nitrogen as well as oxygen of water molecules [41]. According to their quadrupole splitting values, the irons are ascribed in different chemical environments [39,42,43]: 26% of Fe^{II} in octahedral *trans*– $(\text{H}_2\text{O})_2\text{FeN}_4$ and $(\text{H}_2\text{O})\text{FeN}_5$, 32% of Fe^{II} in $(\text{H}_2\text{O})_3\text{FeN}_3$

Table 3
Fractional atomic coordinates and occupancies of $\text{Fe}^{\text{II}}\text{-Co PBA}$.

Wyckoff	Atom	x	y	z	Occ.	$U, \text{\AA}^2$
4a	Co	0	0	0	0.68	0.0347(0)
4b	Fe	0.5	0.5	0.5	1.00	0.052(3)
8c	O1	0.25	0.25	0.25	1.00	0.347(16)
24e	C	0.19	0	0	0.68	0.23(4)
24e	N	0.31	0	0	0.68	0.038(8)
24e	O2	0.23	0	0	0.32	0.15(3)

O1: crystal water, O2: coordinated water.

with H_2O in facial conformation, and 31% Fe^{II} in *cis*– $(\text{H}_2\text{O})_2\text{FeN}_4$ and $(\text{H}_2\text{O})_3\text{FeN}_3$ in meridional conformation. The Rietveld refinements of the XRD patterns of $\text{Fe}^{\text{II}}\text{-Co}$ and $\text{Fe}^{\text{III}}\text{-Co PBA}$ also support this result (Fig. 1 and Fig. S3). The fractional atomic coordinates, occupancies and other related parameters were listed in Table 3 and Table S2, which clearly show the existence of water coordinated irons and the vacancies in the two kinds of Fe–Co PBAs.

Mössbauer spectrum of $\text{Fe}^{\text{II}}\text{-Co PBA}$ after the photo-Fenton reaction (Fig. 7c) gives clear evidence that the major part iron ions (92%) was oxidized and the new Fe–O phase was generated during the photo-Fenton process. It is frequently found in Fenton reactions that the oxidation of ferrous species is usually in a higher rate than the inverse process [39]. Indeed, $\text{Fe}^{\text{III}}\text{-Co PBA}$ with Fe^{III} in octahedrally coordinated structure showed considerable photo-Fenton

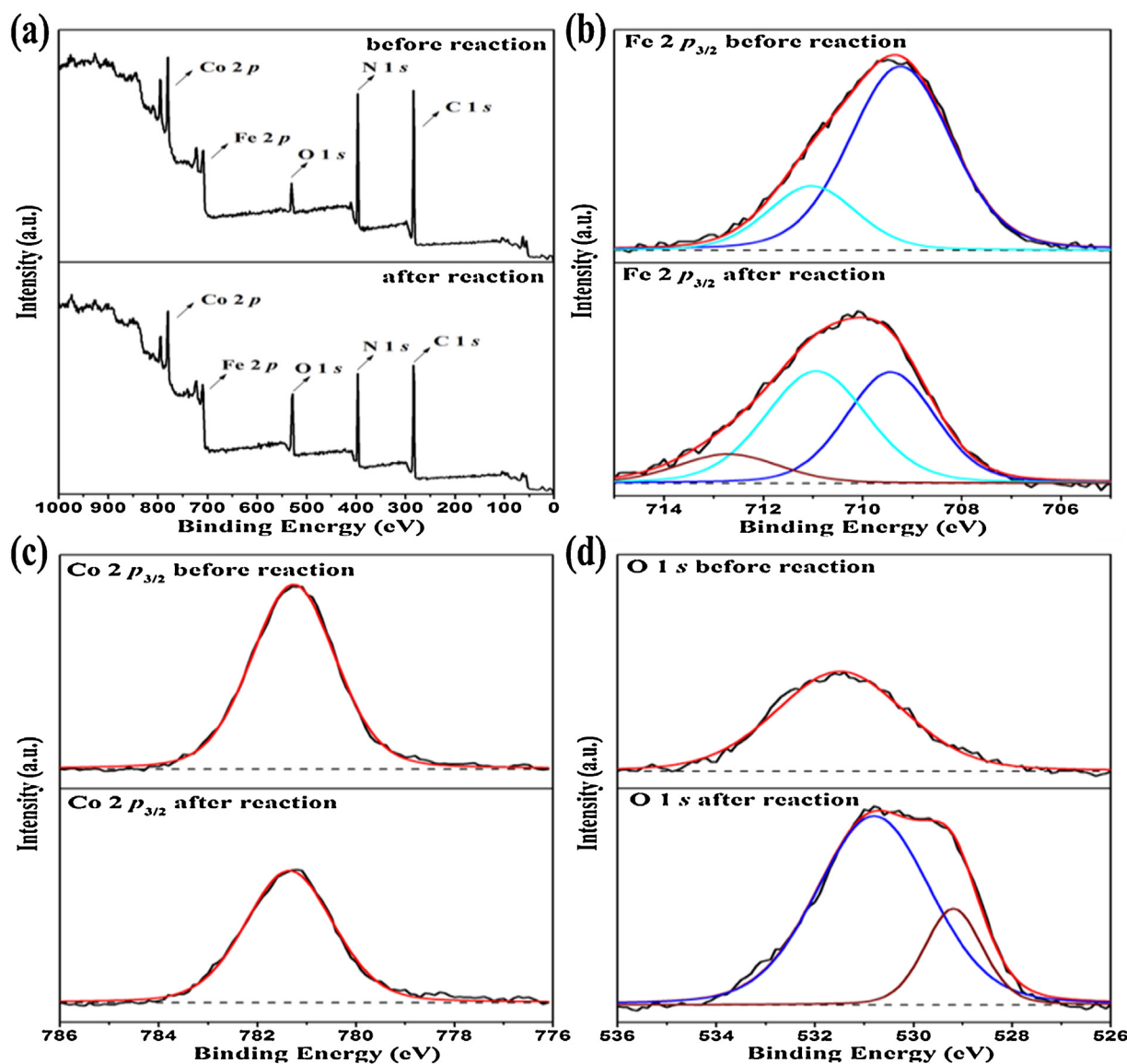


Fig. 6. XPS of Fe^{II}-Co PBA before and after photo-Fenton reactions: (a) The full XPS spectra and the high resolution spectra of (b) Fe 2p_{3/2}, (c) Co 2p_{3/2} and (d) O 1s.

Table 2

Room temperature ⁵⁷Fe Mössbauer parameters of Fe-Co PBAs obtained before and after the photo-Fenton reactions.

Component	Assignment	IS (mm s ⁻¹)	QS (mm s ⁻¹)	Width (mm s ⁻¹)	Area (%)
Fe ^{II} -Co PBA	Fe ^{III}	5/6N & 1/0(H ₂ O)	0.32	0.48	0.51
	Fe ^{II}	1/2trans(H ₂ O) & 5/4N	1.12	0.87	0.37
		3fac(H ₂ O) & 3N	1.13	1.46	0.39
		2cis/3mer(H ₂ O) & 4/3N	1.14	1.88	0.33
Fe ^{II} -Co PBA Fenton pH 5	Fe ^{III}	60/OH	0.37	0.95	0.46
		5/GN & 1/0(H ₂ O)	0.36	0.55	0.42
	Fe ^{II}	1/2trans(H ₂ O) & 5/4N	1.09	1.39	0.43
		2cis/3mer(H ₂ O) & 4/3N	1.07	2.37	0.36
Fe ^{II} -Co PBA Vis-Fenton pH 5	Fe ^{III}	60/OH	0.36	1.02	0.44
		5/6N & 1/0(H ₂ O)	0.36	0.59	0.44
	Fe ^{II}	1/2trans(H ₂ O) & 5/4N	1.11	1.34	0.43
		2cis/3mer(H ₂ O) & 4/3N	1.08	2.30	0.42
Fe ^{II} -Co PBA Vis-Fenton pH 3	Fe ^{III}	60/OH	0.42	1.06	0.43
		5/GN & 1/0(H ₂ O)	0.36	0.62	0.62
	Fe ^{II}	1/2trans(H ₂ O) & 5/4N	1.04	1.35	0.44
		2cis/3mer(H ₂ O) & 4/3N	1.08	2.37	0.33
Fe ^{III} -Co PBA	Fe ^{III}	5/GN & 1/0(H ₂ O)	0.36	0.40	0.69
	Fe ^{II}	x(H ₂ O) & (6-x)N	1.11	2.05	0.42
Fe ^{III} -Co PBA Vis-Fenton	Fe ^{III}	5/6N & 1/0(H ₂ O)	0.36	0.41	0.63
	Fe ^{II}	x(H ₂ O) & (6-x)N	1.13	2.19	0.42

Experimental errors are $\pm 0.02 \text{ mm s}^{-1}$ for isomer shift (IS), $\pm 0.03 \text{ mm s}^{-1}$ for quadrupole splitting (QS) and 1% for relative area. IS is relative to α -iron foil.

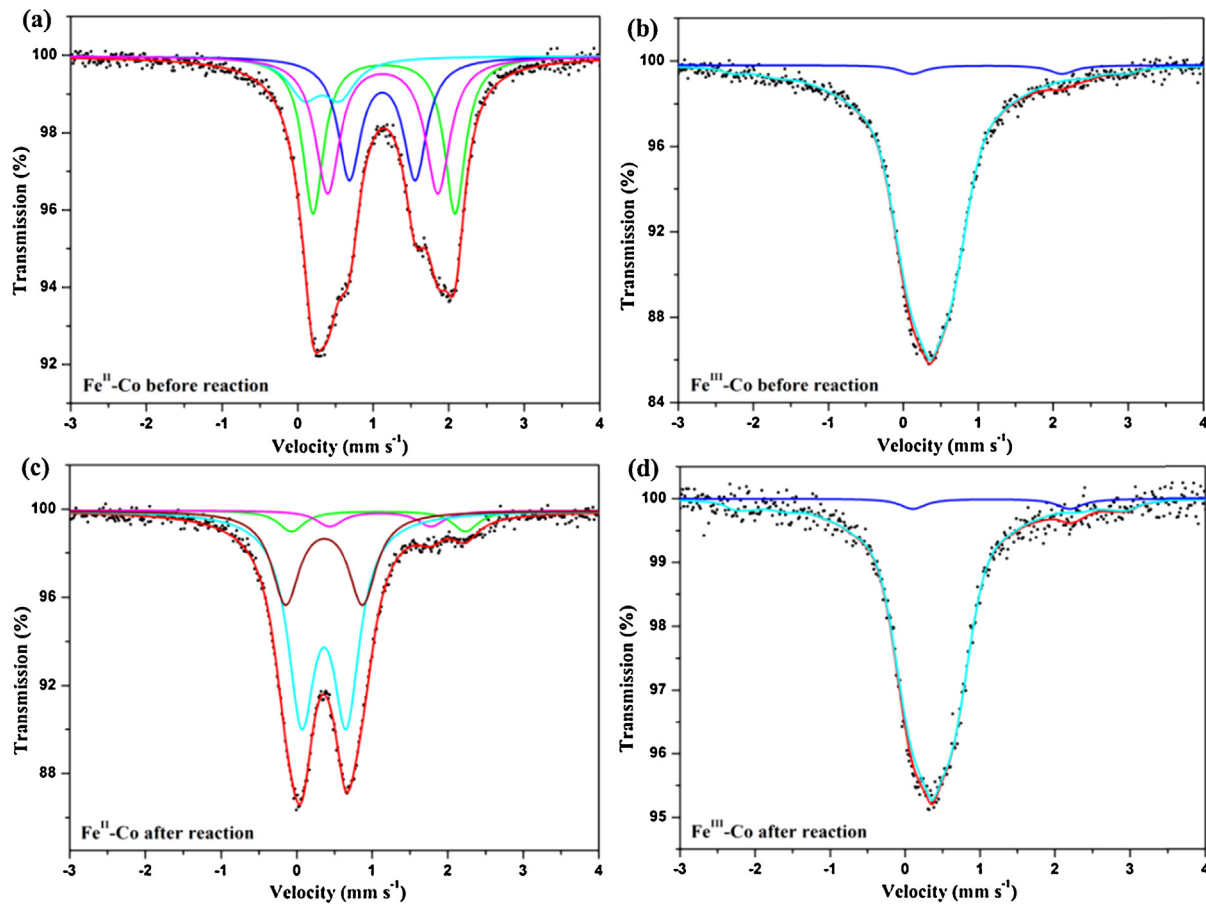
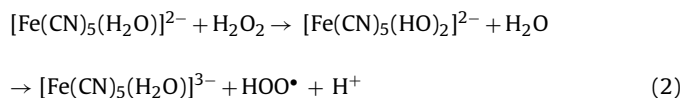
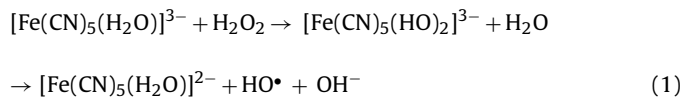


Fig. 7. Room temperature ^{57}Fe Mössbauer spectra of $\text{Fe}^{\text{II}}\text{-Co}$ PBA (a) before, (c) after; $\text{Fe}^{\text{III}}\text{-Co}$ PBA (b) before, and (d) after photo-Fenton reactions. The spectrum of (a) was fitted with four quadrupole doublets. Prevailing external (green color) doublet was assigned to Fe^{II} in octahedral $\text{trans}\text{-}(\text{H}_2\text{O})_2\text{FeN}_4$ and $\text{trans}\text{-}(\text{H}_2\text{O})\text{FeN}_5$ ($1/2\text{trans}(\text{H}_2\text{O}) \& 5/4\text{N}$). Middle doublet (magenta color) was assigned to Fe^{II} in $(\text{H}_2\text{O})_3\text{FeN}_3$ with H_2O in 3D conformation ($3\text{fac}(\text{H}_2\text{O}) \& 3\text{N}$). Inner doublet (blue color) was assigned to $\text{cis}\text{-}(\text{H}_2\text{O})_2\text{FeN}_4$ and $(\text{H}_2\text{O})_3\text{FeN}_3$ with three H_2O in one plane ($2\text{cis}/3\text{mer}(\text{H}_2\text{O}) \& 4/3\text{N}$). The minor doublet (cyan color) represented to the small amount of high-spin Fe^{III} ions in the $\text{Fe}^{\text{II}}\text{-Co}$ PBA. The spectrum of (c) was fitted in the same model as (a) except for the doublet (purple color) assigned to the newly formed Fe-O species after photo-Fenton reaction. The spectra of (b) and (d) were fitted with two quadrupole doublets. The cyan and blue solid lines represent the high-spin Fe^{III} and Fe^{II} components in $\text{Fe}^{\text{III}}\text{-Co}$ PBA, respectively. (For interpretation of the references to color in this figure legend, the reader is referred to the web version of this article.)

activity even though it is lower than $\text{Fe}^{\text{II}}\text{-Co}$ PBA as shown in Fig. 3. The contents of Fe^{II} in $\text{Fe}^{\text{III}}\text{-Co}$ PBA before and after the reaction were both around 4% (Table 2). No obvious difference between the Mössbauer spectra of $\text{Fe}^{\text{III}}\text{-Co}$ PBA before and after the photo-Fenton reaction also suggests that it is quite stable (Fig. 7d). These Mössbauer results made it clear that the iron redox cycling in Fe-Co PBAs occurs during the Fenton processes. The Fe^{II} in Fe-Co PBAs tended to be oxidized by H_2O_2 to produce a new Fe-O phase on the surface of the $\text{Fe}^{\text{II}}\text{-Co}$ PBA nanoparticles. The Fe^{III} could also be reduced by H_2O_2 at a slower rate until the ratio of Fe^{II} and Fe^{III} active sites reached to a certain value. Abundant vacancies and water coordinated iron sites for creating maximal active sites are responsible for the excellent photo-Fenton activities of Fe-Co PBAs.

Generally speaking, at least one coordination position of $\text{Fe}^{\text{II}}/\text{Fe}^{\text{III}}$ sites should be opened or occupied by a labile ligand (such as H_2O) for a homogeneous Fenton reaction to occur [44–46]. The unsaturated or labile ligand coordinated $\text{Fe}^{\text{II}}/\text{Fe}^{\text{III}}$ is considered to preferentially form the Fe-O complexes and then produce the hydroxide radicals [47]. Thus, the plausible mechanisms of photo-Fenton reaction over Fe-Co PBAs can be proposed as follows. Taking the iron ion in $(\text{H}_2\text{O})\text{FeN}_5$ as an example, in the first stage of the Fenton process, the water molecules coordinated to iron sites are replaced by H_2O_2 and form $\text{Fe}^{\text{II}}\text{-peroxide}$ complexes to produce the HO^{\bullet} radicals (Eq. (1)). However, the oxidation of the majority of iron ions (92%) in $\text{Fe}^{\text{II}}\text{-Co}$ PBA should result in releas-

ing some iron ions to form the new Fe-O phase on the surface of $\text{Fe}^{\text{II}}\text{-Co}$ PBA nanoparticles. The Fe^{III} in Fe-Co PBAs could also be reduced by H_2O_2 at a slower rate to produce superoxide radical (HO^{\bullet}) through the formation of $\text{Fe}^{\text{III}}\text{-peroxide}$ complexes (Eq. (2)). In the $\text{Fe}^{\text{II}}\text{-Co}$ PBA, the rate of the reaction expressed by Eq. (2) is not negligible, therefore, the residual Fe^{II} could be always observed by Mössbauer spectroscopy. In the $\text{Fe}^{\text{III}}\text{-Co}$ PBA, the rates of the reactions expressed by Eqs. (1) and (2) should be inversely proportional to the contents of the active sites of Fe^{II} and Fe^{III} , therefore, no change could be observed by Mössbauer spectra. The whole photo-Fenton reaction mechanism over Fe-Co PBAs is shown in Fig. S4. It clearly demonstrates that the abundant water coordinated iron sites within the vacancies of the Fe-Co PBAs structure are the active sites where the Fenton reaction occurs.



The content of Fe^{II} in the $\text{Fe}^{\text{II}}\text{-Co}$ PBA after the photo-Fenton process at pH 4.8 is 11%, higher than that after the dark Fenton reaction (8%), and smaller than that after the photo-Fenton process at pH 3.0

(17%) (Fig. S5). The corresponding Mössbauer spectra are shown in Fig. S6. These results indicate that the enhanced Fenton activity with the assistance of either visible light or low pH is caused by the accelerated reduction of Fe^{III} to Fe^{II}. The most probable reason for this acceleration is that the dyes such as RhB could be excited by visible light irradiation, then it could transfer electron to Fe^{III} (Eqs. (3) and (4)) [48,49].



3.3. Reactive intermediates for Fe–Co PBAs catalyzing photo-Fenton reactions

3.3.1. Radical scavengers

The radical intermediates involved in the photo-Fenton reactions catalyzed by Fe–Co PBAs were probed by using radical scavengers. When TBA, a popular radical scavenger for HO[•] [50], was added to the reaction solution, the RhB degradation efficiency was decreased (Fig. S7), indicating that the hydroxyl radical might be one of the active reaction intermediates. It should also be noted that the reaction was not completely quenched by the addition of TBA, demonstrating that there are also some other radical intermediates involved in the reaction which could not be quenched by TBA. The results of the TBA concentration influence on the RhB degradation efficiency (Fig. S8) further support this assumption. Similar results were obtained when BQ, a scavenger of superoxide radical (HO[•]) [51], was added to the reaction solution. This indicates that HO[•] radical is also an active radical intermediate involved in the reaction, but again it is not the only species since the reaction could not be completely quenched by the addition of BQ. However, when sodium azide, a unique scavenger for singlet oxygen (¹O₂) [52], was added to the reaction mixture, the degradation efficiency of RhB was almost completely quenched, demonstrating that the singlet oxygen plays a key role in the degradation of RhB. The disclosed inhibition effect of BQ and TBA could be rationalized by the fact that completely trapping of the HO[•] or HO[•] would only partially terminate the formation of ¹O₂. This indicates that ¹O₂ produced from HO[•] and HO[•] is directly participated in the degradation of RhB. Thus, the relevant radical reactions can be proposed as shown in Eqs. (5)–(12) [28,53]. The singlet oxygen ¹O₂, acting as the directly active species in RhB degradation, was produced probably by the rapid relevant radical reaction process in the vacancies of the Fe–Co PBAs structure as shown in Fig. S4.



3.3.2. EPR

To further confirm the identity of the reactive intermediates, the EPR/DMPO spin trapping experiments were carried out. This technique is useful to detect the active oxygen species in a photo-Fenton system [54]. The radical adduct DMPOX (5, 5-dimethyl-2-pyrrolidone-N-oxyl, with $a_N = 7.2 \text{ G}$ and $a_{\text{H}}^{\text{r}} = 4.1 \text{ G}$) [55], always generated from the reaction of ¹O₂ with DMPO, was detected in the catl-H₂O₂-aqueous system (Fig. 8) [56], indicating the existence of ¹O₂ in the reaction system. Due to the rapid

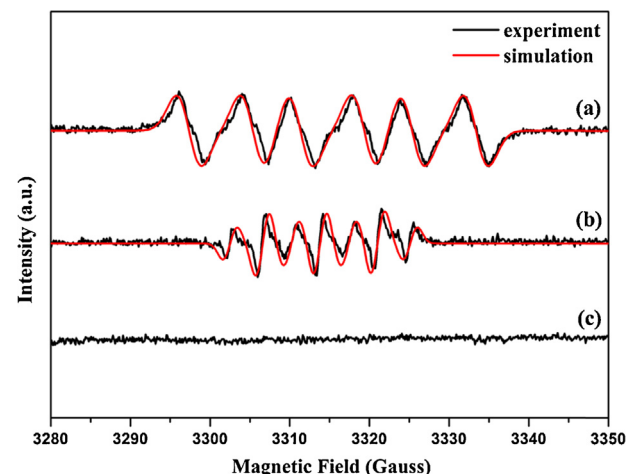


Fig. 8. DMPO trapped EPR spectra of three simulated systems. (a) Catl-H₂O₂-ethanol system; (b) Catl-H₂O₂-aqueous system; (c) H₂O₂-aqueous system.

self-scavenging effect of HO[•] by hydrogen peroxide to produce HOO[•] (Eq. (8)) and the rapid radical reactions to produce ¹O₂ (Eqs. (9)–(11)) [57], no DMPO-•OH was detected. The formation of the HOO[•] radical, which is unstable in aqueous solution, was further confirmed by catl-H₂O₂-ethanol system (Fig. 8). The radical adduct DMPO-•OOH ($a_N = 14 \text{ G}$ and $a_{\text{H}}^{\text{r}} = 8 \text{ G}$) generated from the reaction of HOO[•] with DMPO [58] was detected, indicating formation of HOO[•] through Eqs. (6) and (7). These spin-trap experiments further confirm the plausible radical reactions mechanism of the whole photo-Fenton process over Fe–Co PBAs as shown in Fig. S4.

3.4. Factors influencing the degradation of RhB by Fe–Co PBAs photo-Fenton process

The effect of H₂O₂ concentration on the degradation of RhB was examined and the results are presented in Fig. S9. Even when the H₂O₂ concentration was raised up to one hundred times, the degradation efficiency continued to increase with increasing the H₂O₂ concentration, indicating that more and more active iron sites were participated in the photo-Fenton process. Mössbauer spectroscopy reveals a variety of iron sites coordinated by water with comparable abundances of 32%, 31%, 26% and 11% (Table 2). This result implies that nearly all these iron sites can be served as the active sites, which maximized the available active sites of Fe–Co PBAs in the photo-Fenton process.

Next, the effect of initial pH on the degradation of RhB was investigated and the results are depicted in Fig. S10. The values of k decreased slightly as the solution pH increased to 11.0, this is because the higher pH will restrain the reduction of Fe^{III} to Fe^{II} as proved by Mössbauer spectroscopy. However, the complete degradation of RhB could still be achieved within 30 min even at the initial pH 8.5. This result clearly demonstrated that the validity of the Fe–Co PBAs to degrade organic compounds under a wide pH range. The change of solution pH during the reaction was shown in Fig. S11. It was observed that even at the initial pH 10.4, the pH value of the solution after the photo-Fenton reaction shifted to around 3.5 and further decrease to more acidic without any acidity adjustment, suggesting the generation of HOO[•] radicals in the reaction process (Eq. (8): $pK_a = 4.8 \pm 0.1$) [59].

3.5. The chemical stability and recyclability of Fe–Co PBAs

The stability of the catalyst is an important issue that has to be considered. Therefore, the iron and cobalt leaching in the Fe–Co PBAs photo-Fenton process was analyzed (Fig. S11). According to

the charge balance in the Fe^{II}-Co PBA, the oxidation of the major part iron ions (92%) must result in releasing another part of iron ions. However, the iron concentration in the solution was less than 3 mg L⁻¹ during the whole process. This indicates the direct formation of the new Fe-O species on the surface of the Fe^{II}-Co PBA nanoparticles. The concentration of the cobalt ion released into the solution was reached to about 1.7 mg L⁻¹ after the reaction, suggesting the instability of the Fe^{II}-Co PBA in the photo-Fenton process. However, when the Fe^{III}-Co PBA was used as the photo-Fenton catalyst, no obvious iron and cobalt leaching was detected (less than 0.15 mg L⁻¹). The total cyanide concentration calculated based the concentration of leached cobalt, was less than 0.9 mg L⁻¹, which is within the legal limit (2 mg L⁻¹) imposed by the directives of China. Combine with the result of 51% TOC removal efficiency of RhB by Fe^{III}-Co PBA in 30 min (Fig. S12), it can be concluded that Fe^{III}-Co PBA is a promising photo-Fenton catalyst for the practical application.

The operational stability of Fe^{II}-Co PBA was investigated by testing the degradation efficiency of RhB in consecutive runs as shown in Fig. S13. Because of the oxidation of the major proportion of the iron ions (92%) in Fe^{II}-Co PBA after the first run, the degradation efficiency was significantly reduced in the second run. However, due to the abundance of the active iron sites in Fe-Co PBAs, the degradation efficiency could be resumed to complete degradation of RhB by increasing the H₂O₂ concentration up to 40 mM as shown by the third run. Next, the catalyst regenerated in the photo-Fenton process exhibited good performance in the subsequent four-cycle runs. These results demonstrate the high recyclability of both as-synthesized Fe^{III}-Co PBA and oxidized Fe^{II}-Co PBA.

4. Conclusions

For the first time, the excellent photo-Fenton reaction activities of Fe-Co PBAs are reported in this work. The existence of the highly dispersed water coordinated iron sites and the abundant vacancies in their MOFs structure are responsible for the high activities. Control experiments with different reaction conditions demonstrated the validity of the Fe-Co PBAs to degrade organic compounds under a wide pH range. Comparison of the Fenton reaction activities of Fe^{II}-Co PBA and Fe^{III}-Co PBA shows that the former is more active but the latter is more stable. Combining with a series of characterization techniques, especially with Mössbauer spectroscopy, the iron redox cycling during the whole Fenton process was identified and the mechanisms of the reactions proceeding at the vacancies of the Fe-Co PBAs structure are proposed. Both light irradiation and low pH media were identified to accelerate the reduction of Fe^{III} to Fe^{II} in the Fe-Co PBAs, hence further increase their Fenton reaction activities. The singlet oxygen (¹O₂) produced indirectly from HOO[•] and HO[•] was found to participate directly in the degradation of RhB. Considering the easy synthesis and availability of various transition metals to be incorporated into the structure of PBAs, we think that this work not only opens a new way for the general use of PBAs in photo-Fenton process, but also gives a deeper insight into the heterogeneous Fenton reaction mechanism which is nowadays very limited.

Acknowledgements

This work was supported by the National Natural Science Foundation of China (11079036, 21476232) and also partly supported by the Chinese Academy of Sciences Visiting Professorships for Senior International Scientists (2011T1G15). X. N. Li also thanks Professor Virender K. Sharma of Department of Environmental and Occupational Health, School of Public Health, Texas A&M University, for

his kind guidance and discussion. Many thanks to the anonymous reviewers who have helped improve this paper.

Appendix A. Supplementary data

Supplementary data associated with this article can be found, in the online version, at <http://dx.doi.org/10.1016/j.apcatb.2015.05.033>

References

- [1] A.D. Levine, T. Asano, Environ. Sci. Technol. 38 (2004) 201A.
- [2] M.A. Shannon, P.W. Bohn, M. Elimelech, J.G. Georgiadis, B.J. Marinas, A.M. Mayes, Nature 452 (2008) 301.
- [3] C. Sun, C. Chen, W. Ma, J. Zhao, Phys. Chem. Chem. Phys. 13 (2011) 1957.
- [4] F. Mazille, T. Schoettl, N. Klamert, S. Malato, C. Pulgarin, Water Res. 44 (2010) 3029.
- [5] H.M.H. Gad, A.A. El-Sayed, J. Hazard. Mater. 168 (2009) 1070.
- [6] K. Pazdior, A. Klepacz-Smolka, S. Ledakowicz, J. Sojka-Ledakowicz, Z. Mrozinśka, R. Zyła, Chemosphere 75 (2009) 250.
- [7] S. Papic, N. Koprivancic, A.L. Bozic, D. Vujevic, S.K. Dragievic, H. Kusic, I. Peternel, Water Environ. Res. 78 (2006) 572.
- [8] L. Xu, J. Wang, Environ. Sci. Technol. 46 (2012) 10145.
- [9] Y. Wang, H. Zhao, M. Li, J. Fan, G. Zhao, Appl. Catal. B 147 (2014) 534.
- [10] C. Wang, H. Liu, Z. Sun, Int. J. Photoenergy 2012 (2012) 1.
- [11] S.R. Pouran, A.A.A. Raman, W.M.A.W. Daud, J. Clean Prod. 64 (2014) 24.
- [12] Q. Wang, S. Tian, J. Long, P. Ning, Catal. Today 224 (2014) 41.
- [13] S.-J. Yuan, X.-H. Dai, Appl. Catal. B 154 (2014) 252.
- [14] X.J. Yang, X.M. Xu, J. Xu, Y.F. Han, J. Am. Chem. Soc. 135 (2013) 16058.
- [15] M. Tokumura, R. Morito, R. Hatayama, Y. Kawase, Appl. Catal. B 106 (2011) 565.
- [16] A.D. Purceno, A.P.C. Teixeira, A.B. Souza, J.D. Ardisson, J.P. de Mesquita, R.M. Lago, Appl. Clay Sci. 69 (2012) 87.
- [17] R. Zboril, M. Mashlan, D. Petridis, Chem. Mater. 14 (2002) 969.
- [18] X.N. Li, J. Wang, A.I. Rykov, V.K. Sharma, H.Z. Wei, C.Z. Jin, X. Liu, M.R. Li, S.H. Yu, C.L. Sun, D.D. Dionysiou, Catal. Sci. Technol. 5 (2015) 504.
- [19] O. Sato, T. Iyoda, A. Fujishima, K. Hashimoto, Science 272 (1996) 704.
- [20] S.S. Kaye, J.R. Long, J. Am. Chem. Soc. 127 (2005) 6506.
- [21] S. Margadonna, K. Prassides, A.N. Fitch, J. Am. Chem. Soc. 126 (2004) 15390.
- [22] S. Pintado, S. Goberna-Ferron, E.C. Escudero-Adan, J. Ramon Galan-Mascaro, J. Am. Chem. Soc. 135 (2013) 13270.
- [23] A. Garcia-Ortiz, A. Grirrane, E. Reguera, H. Garcia, J. Catal. 311 (2014) 386.
- [24] M. Takachi, T. Matsuda, Y. Moritomo, J. Appl. Phys. 52 (2013).
- [25] S. Natesakawat, J.T. Culp, C. Matranga, B. Bockrath, J. Phys. Chem. C 111 (2007) 1055.
- [26] A. Derobertis, A. Bellomo, D. Demarco, Talanta 23 (1976) 732.
- [27] R.C.C. Costa, F.C.C. Moura, J.D. Ardisson, J.D. Fabris, R.M. Lago, Appl. Catal. B 83 (2008) 131.
- [28] W. Li, Y. Wang, A. Irini, Chem. Eng. J. 244 (2014) 1.
- [29] C. Bai, W. Gong, D. Feng, M. Xian, Q. Zhou, S. Chen, Z. Ge, Y. Zhou, Chem. Eng. J. 197 (2012) 306.
- [30] P.P. Gan, S.F.Y. Li, Chem. Eng. J. 229 (2013) 351.
- [31] F. Hashemzadeh, R. Rahimi, A. Gaffarnejad, Environ. Sci. Pollut. Res. 21 (2014) 5121.
- [32] L. Ai, C. Zhang, L. Li, J. Jiang, Appl. Catal. B 148 (2014) 191.
- [33] R.R. Sheha, J. Colloid Interface Sci. 388 (2012) 21.
- [34] J.B. Ayers, W.H. Waggoner, J. Inorg. Nucl. Chem. 33 (1971) 721.
- [35] K. Itaya, I. Uchida, V.D. Neff, Acc. Chem. Res. 19 (1986) 162.
- [36] G. Zhao, J.J. Feng, Q.L. Zhang, S.P. Li, H.Y. Chen, Chem. Mater. 17 (2005) 3154.
- [37] W.E. Buschmann, J. Ensling, P. Gutlich, J.S. Miller, Chem. -Eur. J. 5 (1999) 3019.
- [38] D. Ivezkovic, H.V. Trbic, R. Peter, M. Petracic, M. Ceh, B. Pihlar, Electrochim. Acta 78 (2012) 452.
- [39] E. Coronado, M.C. Gimenez-Lopez, T. Korzeniak, G. Levchenko, F.M. Romero, A. Segura, V. Garcia-Baona, J.C. Cezar, F.M.F. de Groot, A. Milner, M. Paz-Pasternak, J. Am. Chem. Soc. 130 (2008) 15519.
- [40] A.I. Rykov, J. Wang, T. Zhang, K. Nomura, Hyperfine Interact. 218 (2013) 53.
- [41] H.U.G. Andreas Ludi, Inorg. Chem. 14 (1973) 1.
- [42] A.I. Rykov, J. Wang, T. Zhang, K. Nomura, Hyperfine Interact. 218 (2013) 139.
- [43] P. Gülich, R. Link, A. Trautwein, Mössbauer Spectroscopy and Transition Metal Chemistry, Springer, Berlin, 2011.
- [44] J.J. Pignatello, E. Oliveros, A. MacKay, Crit. Rev. Environ. Sci. Technol. 36 (2006) 1.
- [45] E. Graf, J.R. Mahoney, R.G. Bryant, J.W. Eaton, J. Biol. Chem. 259 (1984) 3620.
- [46] L. Zhou, Y. Shao, J. Liu, Z. Ye, H. Zhang, J. Ma, Y. Jia, W. Gao, Y. Li, ACS Appl. Mater. Interfaces 6 (2014) 7275.
- [47] H. Gallard, J. De Laat, B. Legube, Water Res. 33 (1999) 2929.
- [48] P.V. Nidheesh, R. Gandhimathi, S.T. Ramesh, Environ. Sci. Pollut. Res. 20 (2013) 2099.
- [49] S. Yuan, X. Dai, Appl. Catal. B 154 (2014) 252.
- [50] J. Benner, T.A. Ternes, Environ. Sci. Technol. 43 (2009) 5472.
- [51] M. Yin, Z. Li, J. Kou, Z. Zou, Environ. Sci. Technol. 43 (2009) 8361.
- [52] L. Ge, J. Chen, J. Lin, X. Cai, Environ. Sci. Technol. 43 (2009) 3101.

- [53] L. Zhou, W. Song, Z. Chen, G. Yin, Environ. Sci. Technol. 47 (2013) 3833.
- [54] H.B. Fu, L.W. Zhang, S.C. Zhang, Y.F. Zhu, J.C. Zhao, J. Phys. Chem. B 110 (2006) 3061.
- [55] M.V. Alipazaga, G. Cerchiaro, H.D. Moya, N. Coichev, J. Braz. Chem. Soc. 20 (2009) 1302.
- [56] J. Ueda, K. Takeshita, S. Matsumoto, K. Yazaki, M. Kawaguchi, T. Ozawa, Photochem. Photobiol. 77 (2003) 165.
- [57] X. Xue, K. Hanna, N. Deng, J. Hazard. Mater. 166 (2009) 407.
- [58] J.H. Ma, W.H. Ma, W.J. Song, C.C. Chen, Y.L. Tang, J.C. Zhao, Y.P. Huang, Y.M. Xu, L. Zang, Environ. Sci. Technol. 40 (2006) 618.
- [59] S. Sabhii, J. Kiwi, Water Res. 35 (2001) 1994.